This is the accepted manuscript made available via CHORUS. The article has been published as:

Long-term adherent cell dynamics emerging from energetic and frictional interactions at the interface

Satoru Okuda and Tetsuya Hiraiwa

Phys. Rev. E **107**, 034406 — Published 17 March 2023

DOI: 10.1103/PhysRevE.107.034406

Long-term adherent cell dynamics emerging from energetic and frictional interactions at the interface

Satoru Okuda[1*], Tetsuya Hiraiwa[2]

[1]Nano Life Science Institute, Kakuma-machi, Kanazawa, Japan

[2]Mechanobiology Institute, National University of Singapore

*** To whom correspondence: satokuda@staff.kanazawa-u.ac.jp**

Abstract: Cell adhesion plays an important role in a wide range of biological situations, including embryonic development, cancer invasion, and wound healing. Although several computational models describing adhesion dynamics have been proposed, models applicable to long-term, large length scale cell dynamics are lacking. In this study, we investigated possible states of long-term adherent cell dynamics in three-dimensional space by constructing a continuum model of interfacial interactions between adhesive surfaces. In this model, a pseudo-interface is supposed between each pair of triangular elements that discretize cell surfaces. By introducing a distance between each pair of elements, the physical properties of the interface are given by interfacial energy and friction. The proposed model was implemented into the model of a nonconservative fluid cell membrane where the cell membrane dynamically flows with turnover. Using the implemented model, numerical simulations of adherent cell dynamics on a substrate under flow were performed. The simulations not only reproduced the previously reported dynamics of adherent cells, such as detachment, rolling, and fixation on the substrate, but also discovered new dynamic states, including cell slipping and membrane flow patterns, corresponding to behaviors that occur on much longer time scales than the dissociation of adhesion molecules. These results illustrate the variety of long-term adherent cell dynamics, which are more diverse than the short-term ones. The proposed model can be extended to arbitrarily shaped membranes, thus being useful for the mechanical analysis of a wide range of long-term cell dynamics where adhesion is essential.

Keywords: Cell mechanics, Cell adhesion, Interfacial energy, Friction, Triangular mesh, Numerical simulation

1. Introduction

The cell behavior in multicellular organisms is significantly affected by contacts with other cells or with extracellular matrices. These contacts involve cell adhesion molecules (CAMs) via either cadherin, integrin, glycoprotein, or other molecules. The adhesion plays mechanical roles in sensing the stiffness of the environment, footing on scaffolds to fix and move the cell position through space, and jointing cells to form tissues. These functions of adhesion are indispensable for the development and maintenance of a multicellular body, e.g., embryonic development, immune defense, and wound healing. The disregulation of this adhesion may yield congenital diseases and cancer invasion. Much information has been obtained at the molecular level about the properties of adhesion molecules, e.g., affinity and lifetime, as well as at the cell and tissue levels about the contribution and necessity of each molecule to each phenomenon. Adherent cell behavior is integrated with other elementary behaviors such as actomyosin contraction, osmotic swelling, and polarity formation, and is incorporated into the overall-cell behavior. Because these elementary behaviors are intricately entangled, it is still unclear how individual elementary behaviors of cells involving adhesion are integrated into the dynamics of a whole cell or cell population.

To quantitatively analyze the dynamics of a whole adherent cell or its population, the time and space scales are particularly attentive to the scale of the target phenomenon. Indeed, there is a large-scale gap from the interface between cells or cell-substrate to the whole cell. The interface includes the cortex, thickness of which is less than $200\ \mathrm{nm}$ [1], and the gap between cells and cell-substrate, width of which is about $40\ \mathrm{nm}$ [2]. On the interface, many CAMs concentrate, e.g., cadherin concentration is about $1.6 \times 10^3 \sim 3.6 \times 10^4\ \mathrm{molecules/\mu m^2}$ [3,4]. In the length scale of a whole cell (about $15\ \mathrm{\mu m}$), the thickness of the interface and the individual-CAM behavior can be ignored. Moreover, notable phenomena of a whole cell or population often occur on time scales of hours to days. Individual CAMs associate and disassociate with a lifetime from 0.1 to 2 seconds to minutes [5], which can also be ignored in the long-time scale of a whole cell or cell population dynamics.

From a macroscopic point of view, CAM behaviors can be simplified into energetic and frictional forces at the interface. Molecular associations generate interfacial energy, which leads to an adsorptive force to keep the two adhered surfaces apart in the normal direction of the interface as well as a negative interfacial tension to extend the interfacial area in the tangential direction. The excluded volume effect of the two adhered surfaces generates a repulsive force to repel the surfaces in the normal direction. In addition, molecular associations and dissociations generate a frictional force between the surfaces. Therefore, at the overall cell-behavioral level, the CAM behaviors can be described by interfacial tension and friction in both normal and tangential directions of the interface.

To analyze complicated deformations of cells in three-dimensional (3D) space, numerical simulations have been increasingly utilized. Many methods have been developed, which can be roughly classified into two types: i) surface-discretization type such as a finite element method [6], boundary element method [7], boundary-integral method [8,9], particle-spring models [10–13], and cell vertex model [14,15], and ii) space-discretization type such as phase-field method [16–19] and cellular Potts model [19–22]. Since surface-discretization methods explicitly describe the surface geometry, the stress exerted on the surface can be directly calculated. On the other hand, surface-discretization methods require some additional tricks to deal with interfacial interactions between contacting surfaces. In contrast, space-discretization methods implicitly describe the surface geometry as an interface between different phases and as an interface between lattice sites with different states, respectively. Space-discretization methods can directly calculate the movement of surfaces and can easily represent the complicated, large deformation of the cell. However, because space-discretization methods represent the interface as a continuous space between pseudo-phases and as a stochastic boundary between two states, respectively, the stress exerted on each surface cannot be directly calculated. In addition, in phase-field models, the frictional force between contacting surfaces cannot be explicitly taken into account because the phase has a viscosity both in the phase and at the interface which cannot be distinguished. Cellular Potts models have the same difficulty in taking into account the frictional force in the state interface. Thus, surface- and space-discretization methods differ significantly in their descriptions of the interface dynamics.

To address the roles of adhesion in cell dynamics, numerical simulations using surface-discretization methods have been used, which especially utilize either discrete models based on spring bonds [23–26] or continuum models based on contacts between elastic bodies [27,28]. The discrete models explicitly describe individual adhesion molecules by bonds with certain lengths, and the association and dissociation process of each molecule by connecting and disconnecting a bond. However, there is a gap of spatial and temporal scales from the individual-CAM behavior to the whole-cell behavior. The pioneering work proposed a continuum model that describes cell adhesion based on contact mechanics and successfully reproduces repulsive and adsorptive interactions between curved surfaces [27]. However, in this continuum model, the property of each cell is assumed to be an elastic body and only the normal force to the interface is taken into account. Therefore, there is a lack of computational methods based on continuum models that explicitly describe interfacial energy and friction, which are crucial for properly simulating adherent cell dynamics at long-term and large-length-scale as mentioned above.

In this paper, we computationally investigated possible states of long-term adherent cell dynamics in 3D space by constructing a simple continuum model of interfacial interaction between adhesive surfaces. In this model, a pseudo-interface is supposed between each pair of triangular elements that discretize cell surfaces. By introducing a distance between each pair of elements, the physical properties of the interface are given by interfacial energy and friction. The proposed model of adhesion was implemented into the model of a cell membrane that takes into account the dynamic flow and turnover of the membrane, whose non-conservative feature is another essential factor in long-term cell dynamics [29]. Using the implemented model, numerical simulations of adherent cell dynamics on a substrate under flow were performed. The simulations not only reproduced several patterns of adherent cell dynamics reported in literature, but also discovered new dynamic states that correspond to behaviors that occur on much longer time scales than the dissociation of adhesion molecules.

2. Brief review: Description of long-term cell dynamics with membrane turnover

In this article, we first construct the model of long-term cell dynamics with adhesion by implementing the continuum model of cell adhesion into the description of long-term cell surface dynamics with turnover, which we proposed previously [29]. Before introducing our cell-adhesion model, in this section, we review the description of cell surface dynamics briefly.

The proposed model of cell adhesion has the advantage of being able to describe long-term, large-scale behaviors of adhesion. Therefore, we employed a model of cell dynamics that we previously proposed, which can be applied to the long-term dynamics of a whole cell [29]. This model describes the fluidic and nonconservative feature of the cell surface membrane, i.e., the membrane dynamically flows with a turnover such as polymerization and depolymerization of cortical actin. In this model, the cell surface membrane is discretized by a triangular mesh, which is a unifying element for describing the 3D shape of a cell (Fig. 1a-b). To introduce cell adhesion into this model, each triangle is further discretized into four elements of similar triangles (Fig. 1c). In this section, we briefly outline this model.

For long-term cell dynamics over tens of minutes, the effects of convection and inertia can be ignored due to the small Reynolds number. By ignoring the inertia term in the Stokes equation, the governing equation of a membrane with a velocity vector $\boldsymbol{u}$ is expressed as

$$\mu \nabla^2 \boldsymbol{u} = \boldsymbol{f}. \tag{1}$$

In Eq. (1), the left-hand term indicates viscous force per area on the membrane. The constant μ indicates the planar viscous coefficient of the cell surface membrane involving the cell cortex, i.e., the viscous coefficient in the planar direction of the membrane. In Eq. (1), the normal viscosity, i.e., the viscosity in the direction along membrane thickness is ignored, and the shear and dilational components of the planar viscous coefficients are assumed to have the same value. The right term, $\boldsymbol{f}$, represents the external force per area.

To discretize the viscous force on the triangular mesh describing the cell surface, $\mu\nabla^2\boldsymbol{u}$, in Eq. (1), the discrete type of the Laplace-Beltrami operator [30] is applied. By introducing an arbitrary parameter, represented by ϕ, the Laplacian operator at $\boldsymbol{r}_i$ is given by

$$\langle\nabla^2\phi\rangle_i \equiv \frac{1}{2A^*}\sum_{j\neq i}\left(\cot\alpha_{ij}+\cot\beta_{ij}\right)\left(\phi_i-\phi_j\right), \tag{2}$$

where ϕ_i is the value of the arbitrary parameter around the i-th vertex. Here, constant A^* is the representative surface area around individual vertices [31]. Variables α_{ij} and β_{ij} are the diagonal angles to the *ij*th edge within the triangles sharing the *ij*-th edge [31]. Moreover, the external force, $\boldsymbol{f}$, in Eq. (1) is discretized into the forces on the vertices. The external force comprises the energetic force from cell behaviors and the viscous force from the environment, which are defined with an energy function, U, and a dissipation function, W, respectively. Therefore, Eq. (1) can be rewritten as

$$\mu\langle\nabla^2\boldsymbol{u}\rangle_i = -\rho_*\frac{\partial U}{\partial\boldsymbol{r}_i} - \rho_*\frac{\partial W}{\partial\boldsymbol{u}_i}. \tag{3}$$

The left-hand side in Eq. (3) indicates the viscous force around the i-th vertex. The first and second terms on the right-hand side indicate the energetic and viscous forces per area around the i-th vertex, respectively. The constant ρ_* is the mean numeric density of vertices on the membrane.

In Eq. (3), energetic forces involving active force that cells generate described by the function of U, such as the osmotic pressure, surface tension, bending moment, and cell-cell adhesion, are introduced. By representing the i-th vertex location by $\boldsymbol{r}_i$ ($\boldsymbol{u}_i = \partial\boldsymbol{r}_i/\partial t$) and the active parameter by a_i around the i-th vertex, U is given as

$$U = U(\{\boldsymbol{r}_i\},\{a_i\}), \tag{4}$$

where { } indicate a set of values. Viscous forces on cell membrane from the environment, such as a viscous resistance from solvent and other cells, are described by the function of W. Using $\boldsymbol{r}_i$ and $\boldsymbol{u}_i$, W is given as

$$W = W(\{\boldsymbol{r}_i\},\{\boldsymbol{u}_i\}). \tag{5}$$

3. Continuum modeling of interfacial interactions between adhesive surfaces

In this section, we propose a coarse-grained model that describes interfacial interactions between arbitrary elements such as triangles, which in principle is generally applicable to the surface-discretization methods. To develop the model, the total area and energy of the interface between two surfaces are described as the summations among discrete elements (Section 3.1). By considering a pseudo-interface between each pair of the elements, normal and tangential distances between each pair are introduced (Section 3.2). Using these distances, interfacial energy and dissipation functions can be defined (Section 3.3). The physical parameters of the interface on the continuum level can be described by those on the molecular level (Section 3.4).

3.1 Interfacial energy between contact surfaces

Surfaces contact each other to form an interface. The α-th and β-th surfaces are represented by S_α and S_β, on which position vectors are represented by $\boldsymbol{x}_\alpha$ and $\boldsymbol{x}_\beta$, respectively (Fig. 1a). By ignoring the thickness of surfaces, the interface can be defined to be at the position where cell surfaces overlap ($\boldsymbol{x}_\alpha = \boldsymbol{x}_\beta$). The area of the interface between the α-th and β-th surfaces, represented by $A_{\alpha\beta}$, can be written by

$$A_{\alpha\beta} = \oint_{S_\beta} \oint_{S_\alpha} \delta(\boldsymbol{x}_\alpha - \boldsymbol{x}_\beta) dS_\alpha \, dS_\beta, \tag{6}$$

where δ is the Dirac delta function. The interfacial energy between the α-th and β-th surfaces, represented by $U_{\alpha\beta}^{\mathrm{int}}$, can be written by

$$U_{\alpha\beta}^{\mathrm{int}} = \oint_{S_\beta} \oint_{S_\alpha} \epsilon(\boldsymbol{x}_\alpha, \boldsymbol{x}_\beta) \delta(\boldsymbol{x}_\alpha - \boldsymbol{x}_\beta) dS_\alpha \, dS_\beta, \tag{7}$$

where $\epsilon(\boldsymbol{x}_\alpha, \boldsymbol{x}_\beta)$ is the interfacial energy density on $\boldsymbol{x}_\alpha$ $(= \boldsymbol{x}_\beta)$.

Cell surfaces are discretized by elements such as triangles. The surfaces of the i-th and j-th elements are represented by S_i and S_j, on which position vectors are represented by $\boldsymbol{x}_i$ and $\boldsymbol{x}_j$, respectively. The area of the interface between the i-th and j-th elements, represented by A_{ij}, is written by

$$A_{ij} = \oint_{S_j} \oint_{S_i} \delta(\boldsymbol{x}_i - \boldsymbol{x}_j) dS_i \, dS_j. \tag{8}$$

Assuming that the energy density is homogenous within each interface between two elements, the interfacial energy density between the i-th and j-th elements, represented by ϵ_{ij}, can be written by

$$\epsilon_{ij} \equiv \epsilon(\boldsymbol{x}_\alpha \in S_i, \boldsymbol{x}_\beta \in S_j). \tag{9}$$

Using Eqs. (8) and (9), the interfacial energy between the α-th and β-th cells, $U_{\alpha\beta}^{\mathrm{int}}$, can be rewritten by

$$U_{\alpha\beta}^{\mathrm{int}} \approx \sum_{j(\beta)}^{\mathrm{elmnt}} \sum_{i(\alpha)}^{\mathrm{elmnt}} \epsilon_{ij} A_{ij}, \tag{10}$$

where the summation is for all elements within each cell. Therefore, the interfacial energy is described by the energy density and area of the interface.

3.2 Pseudo-interface between discrete surfaces

While the interface was defined to be at the location where surfaces overlap ($\boldsymbol{x}_\alpha = \boldsymbol{x}_\beta$), this definition is too rigorous to express the interface between discrete surfaces such as triangular meshes. To deal with the interface in the discrete description, the position of the pseudo-interface is defined. That is, we consider a pseudo-interface between the i-th and j-th elements, represented by H_{ij}, whose effects on each element are expressed as dependences on the distance in H_{ij} between the i-th and j-th elements (Fig. 2b). Here, we introduced normal vectors of the i-th and j-th elements, represented by $\boldsymbol{n}_i$ and $\boldsymbol{n}_j$. The normal vector of H_{ij}, represented by $\boldsymbol{p}_{ij}$, is defined as

$$\boldsymbol{p}_{ij} \equiv \begin{cases} \dfrac{\boldsymbol{n}_i - \boldsymbol{n}_j}{|\boldsymbol{n}_i - \boldsymbol{n}_j|} & \boldsymbol{n}_i \neq \boldsymbol{n}_j \\ \dfrac{\boldsymbol{c}_j - \boldsymbol{c}_i}{|\boldsymbol{c}_j - \boldsymbol{c}_i|} & \boldsymbol{n}_i = \boldsymbol{n}_j \end{cases}. \tag{11}$$

Using Eq. (11), the distance between the i-th and j-th elements is separated into its normal and tangential components, represented by $d_{ij}^{\perp}$ and $d_{ij}^{\parallel}$, respectively. Components $d_{ij}^{\perp}$ and $d_{ij}^{\parallel}$ are given by

$$d_{ij}^{\perp} = \boldsymbol{p}_{ij} \cdot (\boldsymbol{c}_j - \boldsymbol{c}_i), \tag{12}$$

and

$$d_{ij}^{\parallel} = |(\boldsymbol{c}_j - \boldsymbol{c}_i) - (\boldsymbol{p}_{ij} \cdot [\boldsymbol{c}_j - \boldsymbol{c}_i])\boldsymbol{p}_{ij}|, \tag{13}$$

where $\boldsymbol{c}_i$ and $\boldsymbol{c}_j$ are the center vectors of the i-th and j-th elements. Using Eqs. (12) and (13), each of ϵ_{ij} and A_{ij} was given by a function of each of $d_{ij}^{\perp}$ and $d_{ij}^{\parallel}$, respectively. Variable $d_{ij}^{\perp}$ is positive when the i-th and j-th elements are apart and is negative when they penetrate each other. When $\boldsymbol{n}_i$ and $\boldsymbol{n}_j$ are facing each other, $\boldsymbol{p}_{ij}$ is oriented in the intermediate direction between the i-th and j-th element surfaces. As $\boldsymbol{n}_i$ becomes closer to $\boldsymbol{n}_j$, $\boldsymbol{p}_{ij}$ approaches along $\boldsymbol{c}_j - \boldsymbol{c}_i$, leading to $d_{ij}^{\perp} = |\boldsymbol{c}_j - \boldsymbol{c}_i|$ and $d_{ij}^{\parallel} = 0$.

3.3 Energy and dissipation functions of pseudo-interface

The energy density of the interface between the i-th and j-th elements, ϵ_{ij}, was given by

$$\epsilon_{ij}(d_{ij}^{\perp}) \equiv \epsilon_{\text{int}} \psi_{ij}^{\text{E}}, \tag{14}$$

where the constant ϵ_{int} is the characteristic energy density of the interface, i.e., the adhesion energy density between cell surfaces. Function ψ_{ij}^{E} is a dimensionless scalar function of $d_{ij}^{\perp}$, indicating the strength of the energetic interaction between the i-th and j-th elements. By borrowing the formulation of the Lennard-Jones potential, function ψ_{ij}^{E} was given by

$$\psi_{ij}^{\text{E}} \equiv \left(\frac{d_0^{\perp}}{d_{ij}^{\perp} + d_0^{\perp}}\right)^{12} - 2\left(\frac{d_0^{\perp}}{d_{ij}^{\perp} + d_0^{\perp}}\right)^{6} \quad , \tag{15}$$

where constant $d_0^{\perp}$ indicates the depth of interface. The interfacial energy density becomes $-\epsilon_{\text{int}}$, when the normal component of the distance between the i-th and j-th elements is zero ($d_{ij}^{\perp} = 0$). The function ζ is set to zero when $d_{ij}^{\perp}$ exceeds a cutoff length of $5d_0^{\perp}$.

The area of the interface between two elements is expressed by introducing a weight function of the tangential distance between elements, $d_{ij}^{\parallel}$. The weight of the interface between the i-th and j-th elements, represented by w, was given by

$$w(d_{ij}^{\parallel}) \equiv \begin{cases} 1 - \dfrac{d_{ij}^{\parallel}}{d_0^{\parallel}}, & d_{ij}^{\parallel} < d_0 \\ \quad 0, & d_{ij}^{\parallel} \geq d_0 \end{cases}, \tag{16}$$

where constant $d_0^{\parallel}$ indicates the representative width of individual elements. That is, the interaction between the i-th and j-th elements decreases as their tangential distance increases and disappears when it is greater than d_0. Futhermore, to estimate the total weight for each element, we considered a situation where two planar surfaces were in parallel contact and focused on the contribution from the elements of one surface to an element of the other surface (Fig. 2c). By expressing the representative surface area of individual elements in terms of A_{e}, the average number density of elements distributed on the surface is $1/A_{\text{e}}$. By denoting the distance from the element by r, the average weight density at r can be written by $w(r)/A_{\text{e}}$. Therefore, by integrating the weight density on the surface, the total weight for each element, represented by w_{t}, can be estimated as

$$w_{\mathrm{t}} \equiv \int_{0}^{+\infty} 2\pi r\left(\frac{w(r)}{A_{\mathrm{e}}}\right) dr. \tag{17}$$

Using Eqs. (16) and (17), the area of the interface between the i-th and j-th elements, A_{ij}, was given by

$$A_{ij} \equiv A_{\mathrm{e}}\frac{w\left(d_{ij}^{\parallel}\right)}{w_{\mathrm{t}}}. \tag{18}$$

By substituting Eq. (14) into Eq. (10) and integrating it for all elements in the system, the total interfacial energy in the system, represented by U^{int}, can be written by

$$U^{\mathrm{int}} \equiv \sum_{i}^{\mathrm{elmnt}}\sum_{j(>i)}^{\mathrm{elmnt}} \epsilon_{\mathrm{int}}\zeta_{ij}A_{ij}. \tag{19}$$

Similarly, the dissipation function in the system can be written by

$$W^{\mathrm{int}} \equiv -\sum_{i}^{\mathrm{elmnt}}\sum_{j(>i)}^{\mathrm{elmnt}} \frac{\xi_{\mathrm{int}}\psi_{ij}^{\mathrm{D}}}{2}A_{ij}\left(\boldsymbol{u}_i - \boldsymbol{u}_j\right)^2, \tag{20}$$

where the constant ξ_{int} is the characteristic friction coefficient density. Function ψ_{ij}^{D} is a dimensionless scalar function of $d_{ij}^{\perp}$, indicating the strength of the frictional interaction between the i-th and j-th elements. By borrowing the formulation of the Lennard-Jones potential, function ψ_{ij}^{D} was given by

$$\psi_{ij}^{\mathrm{D}} \equiv \left(\frac{d_0^{\perp}}{d_{ij}^{\perp} + d_0^{\perp}}\right)^7, \tag{21}$$

where the exponent 7 is derived from the first term of the derivative of Eq. (15). The effective friction density coefficient in Eq. (20) becomes ξ_{int}, when the normal component of the distance between the i-th and j-th elements is zero ($d_{ij}^{\perp} = 0$). The relationship between the exponents in Eqs. (15) and (21) leads to the effect that the vertex velocity, which is determined by the balance between energetic and dissipative forces, decreases as $d_{ij}^{\perp}$ becomes shorter. This effect is similar to that used in the model of particle interactions in the dissipative particle dynamics (DPD) method [32].

3.4 Relation from molecular to continuum properties

To clarify the CAM behaviors that determine the continuum property of interface, we consider the association-dissociation of the process of CAM. Based on the general definition of equilibrium constant, given the α-

th and β-th surfaces have CAM concentrations of c_α and c_β, respectively, the concentration of associated molecules, represented by $c_{\alpha\beta}$, is written by

$$c_{\alpha\beta} \equiv \left(\frac{K_{\mathrm{on}}}{K_{\mathrm{off}}}\right) c_\alpha c_\beta, \tag{22}$$

where K_{on} and K_{off} are the association and dissociation constants. Interfacial energy is the summation of the association energy of individual associated molecules. Thereby, interfacial energy is given by

$$\epsilon_{\mathrm{int}} = c_{\alpha\beta} \Delta g, \tag{23}$$

where Δg is the free energy gap of individual molecules before and after association. In addition, by assuming the dissociation rate of each molecule is independent of its strain, the friction density coefficient between the α-th and β-th surfaces is approximately given by

$$\xi_{\mathrm{int}} = \frac{c_{\alpha\beta} E}{K_{\mathrm{off}}}, \tag{24}$$

where E is the spring constant of individual molecules [33]. Using Eqs. (22-24), the constant for the interface property specific to each type of cross-linking CAMs, represented by φ_{int}, can be defined as the ratio of ϵ_{int} to ξ_{int}:

$$\varphi_{\mathrm{int}} = \frac{\epsilon_{\mathrm{int}}}{\xi_{\mathrm{int}}} = \frac{\Delta g K_{\mathrm{off}}}{E}. \tag{25}$$

4. Introducing interfacial interactions into the long-term cell dynamics model

The novelty of the proposed model lies in the continuum description of both energetic and frictional interactions at the interface, which can be applied to the long-term, large length scale dynamics of cell adhesion. To demonstrate the applicability of the proposed model, we performed numerical simulations of adherent cell dynamics on a substrate under shear flow. For this purpose, the proposed model, described in Section 3, was introduced into the model of cell dynamics, described in Section 2 (Section 4.1). In addition, initial and boundary conditions, including a solid substrate and shear flow, were introduced (Section 4.2). This integrated model can be applied to the long-term dynamics of an adherent cell and the physical parameters of the interface can be varied based on those of CAMs (Section 4.3). The integrated model can be implemented for numerical simulations (Section 4.4).

4.1 Energy and dissipation functions for overall cell behavior

To apply the proposed model to cell adhesion dynamics, U in Eq. (3) was expressed as

$$U \equiv \frac{1}{2}K\left(\frac{V}{V_{\mathrm{ref}}}-1\right)^2 + \sum_{i}^{\mathrm{vertex}} \Gamma A_i + \sum_{i}^{\mathrm{elmnt}}\sum_{j(>i)}^{\mathrm{elmnt}} \epsilon_{\mathrm{int}}\zeta_{ij}A_{ij} \quad . \tag{26}$$

The first term indicates the energy of cell volume elasticity, where constant K is the volume elastic modulus. Variable V and constant V_{ref} are the current and reference volumes of the cell, respectively. The second term in Eq. (26) indicates the surface energy of the cell membrane, where constant Γ is the surface tension and variable A_i is the local surface area around the i-th vertex, given by $A_i = \sum_{j(i)}^{\mathrm{triangle}} a_j/3$, where a_j is the area of the j-th triangle that comprises the i-th vertex. The third term in Eq. (26) indicates the adhesion energy between the cell and substrate, where ϵ_{int} is the adhesion energy density between the cell and the substrate. Moreover, W in Eq. (3) was expressed as

$$W \equiv \sum_{i}^{\mathrm{vertex}} \frac{\xi_{\mathrm{e}}}{2}(\boldsymbol{u}_i-\boldsymbol{u}_{\mathrm{e}})^2 + \sum_{i}^{\mathrm{elmnt}}\sum_{j(>i)}^{\mathrm{elmnt}} \frac{\xi_{\mathrm{int}}}{2}\psi_{ij}A_{ij}\left(\boldsymbol{u}_i-\boldsymbol{u}_j\right)^2. \tag{27}$$

The first term indicates the viscous dissipation between the cell and the solvent. Constant ξ_{e} is the friction density coefficient and $\boldsymbol{u}_{\mathrm{e}}$ is the velocity of the solvent on the cell surface. The second term indicates the viscous dissipation between the cell and the substrate, where constant ξ_{int} is the friction density coefficient.

4.2 Condition for cell adhesion on substrate under shear flow

To demonstrate the applicability of the proposed model, numerical simulations of cell dynamics on a solid substrate under a steady flow were performed. The system box was considered, which is rectangular within $0 \le x \le L_x$, $0 \le y \le L_y$, and $0 \le z \le L_z$ in the orthogonal xyz-coordinates (Fig. 3). Periodic boundary conditions were applied to the boundary planes. Additionally, a solid substrate was located at $z = 0$ in the xy-plane.

Under the initial condition, a single cell with a spherical shape was located on the substrate with a slight gap. Both the cell and the substrate were expressed by a triangular mesh, which was pre-randomized and optimized before the simulations. During the simulations, vertex locations and mesh topologies of the cell were dynamically changed, whereas those of the substrate were fixed in coordinates.

A simple shear flow was introduced along the x-axis, whose velocity linearly increases with the distance from the substrate along the z-axis, i.e., the environmental velocity was given by $\bar{\boldsymbol{u}}_{\mathrm{e}} = \dot{\gamma}_{\mathrm{e}} z$, where the constant $\dot{\gamma}_{\mathrm{e}}$ is the shear strain rate. For simplification, the flow field of the solvent around the cell was approximately given by the tangential component of $\bar{\boldsymbol{u}}_{\mathrm{e}}$ on the cell surface, i.e., the solvent velocity on the cell surface in Eq. (27) was simply set to $\boldsymbol{u}_{\mathrm{e}} = \bar{\boldsymbol{u}}_{\mathrm{e}} - (\bar{\boldsymbol{u}}_{\mathrm{e}} \cdot \boldsymbol{n}_i) \ \boldsymbol{n}_i$, where $\boldsymbol{n}_i$ is the normal vector of the cell surface at the i-th vertex. To analyze the effects of solvent flow on cell dynamics, the shear strain rate of solvent, $\dot{\gamma}_{\mathrm{e}}$, was replaced by the capillary number, represented by C_a, which was introduced as

$$C_a \equiv \frac{\xi_{\mathrm{e}} \dot{\gamma}_{\mathrm{e}} d}{\Gamma}, \tag{28}$$

where d is the characteristic diameter of the cell, given by $d = (6V/\pi)^{1/3}$.

4.3 Non-dimensionalization and physical parameter values

By considering a regular triangle with the average area of the triangular mesh, the length of each edge composing the regular triangle is represented by l. Using l, the representative surface area of individual vertices and the representative vertex density per area are written by $A^* = \sqrt{3}l^2/2$ and $\rho_* = 2/\sqrt{3}l^2$, respectively. The physical parameters were non-dimensionalized by length l,energy Γl^2, and time $\tau = \mu/\Gamma$, by fixing the values of l, Γ, and μ. Physical parameters used for the simulations are listed in Table 1 and denoted by dimensionless values in figures. The representative surface area of elements in Eq. (17) is given by the average area of triangular elements as $A_{\mathrm{e}} = \sqrt{3}l^2/16$.

Unit length, l, was determined based on the reference cell volume, V_{ref}. Because cell volumes widely vary with cell types and states, we considered the typical size of HeLa and MDA MB231 cells with about $15 \sim 17 \mu\mathrm{m}$ as examples [34]. Hence, the cell volume was set to about $V_{\mathrm{ref}} = 4 \times 10^3 \mu\mathrm{m}^3$. By fixing $V_{\mathrm{ref}} = 10^3 l^3$, the unit length was set to $l = 1.6 \mu\mathrm{m}$.

Unit energy, Γl^2, was determined based on the cortical tension, Γ. Cortical tension widely varies with cell types and states in $30 \sim 4000 \mathrm{pN}/\mu\mathrm{m}$ (summarized in [35]); for example, HeLa cells increase their surface tension from 0.2×10^3 pN/μm during interphase to 1.6×10^3 pN/μm during metaphase [36]. By considering the property in the interphase, the surface energy density was set to $\Gamma = 10^2 \mathrm{pN}/\mu\mathrm{m}$.

Unit time, τ, was determined based on the planar viscous coefficient of the membrane, μ. The timescale of cortex flow is of the order of tens of seconds, for example, cortical actins typically turn over within a few tens of seconds [37,38], which gives an expected planar viscosity of $\mu = 10^3 \mathrm{pNs}/\mu\mathrm{m}$ for the cortex [35]. The main component of the solvent for cells is water, whose viscosity is $0.69 \ \mathrm{pNs}/\mu\mathrm{m}^2$, from which the friction density coefficient of a triangular element with the length size of l in the solvent was approximately set to $\xi_{\mathrm{e}} = 1$ pNs/μm $(10^{-3}\ \mu)$, much lower than the other viscous effects.

Volume elasticity of cells widely varies with cell states; for example, HeLa cells increase their internal hydrostatic pressure from 40 pN/μm during interphase to 400 pN/μm during metaphase [36], whereas cell volumes are maintained to some extent. For simplification, by assuming the incompressibility of cytoplasm, the elastic modulus of cell volume was set to $K = 2.6 \times 10^{7}$pN. μm $(10^{5}\Gamma l^{2})$, much higher than the other energetic effects. The remaining parameters in the system were ϵ_{int}, ξ_{int}, and C_a.

The adhesion energy density, ϵ_{int}, can be written by $\epsilon_{\mathrm{int}} = c\Delta g$ using Eq. (23), where c is the number density of associated adhesion molecules and Δg is the association energy. Both c and Δg vary with the CAM type; for example, the adhesion energy of each cadherin bond is about $\Delta g = 2{\sim}8k_BT$ [39]. Cadherin density is estimated from experiments, where the reported values are about $c = 1.4 \times 10^{4} \sim 3.6 \times 10^{4}$ molecules/μm^2 on adherens junctions [3] and $1.6 \times 10^{3} \sim 1.2 \times 10^{4}$ molecules/μm^2 on migrating cell surfaces [4], giving the adhesion energy density of $\epsilon_{\mathrm{int}} = 110 \sim 1200$ pN/μm $(1.1{\sim}12\ \Gamma)$ and $\epsilon_{\mathrm{int}} = 0.16{\sim}0.38$ pN/μm $(0.0016{\sim}0.0038\ \Gamma)$. Hence, in our simulations, the adhesion energy density was varied in the range of $10^{-3}\ \Gamma \leq \epsilon_{\mathrm{int}} \leq 10\ \Gamma$.

The constant for the interface property specific to each type of cross-linking CAMs, φ_{int}, can be written by Eq. (25). The spring constant of each cadherin is about $E = 35$ pN/μm [40] and the dissociation rate is about $0.2{\sim}1.6\ \mathrm{s}^{-1}$ or much lower [5,41–43]. Using Eq. (25), the constant φ_{int} is roughly estimated as $\varphi_{\mathrm{int}} = 0.05 \times 10^{-3}{\sim}1.5 \times 10^{-3}$ μm$^2/s$ $(0.2 \times 10^{-3}\ l^2/\tau\ {\sim}6 \times 10^{-3}\ l^2/\tau)$ or much lower. For simplification, the constant φ_{int} was set to $\varphi_{\mathrm{int}} = 10^{-2}\ l^2/\tau$ $(2.56 \times 10^{-3}$μm$^2/s)$. In this situation, the characteristic relaxation time of the adhered interface can be estimated to range from roughly $1/c\varphi_{\mathrm{int}} = 0.02\ s$ for typical CAM densities to infinitely large values in the absence of CAMs, whereas the relaxation time of the cell membrane lined by actomyosin cortex can be roughly estimated to $\mu/\Gamma = 10$ s. Thus, the adhesion interface can be relaxed on both much faster and slower time scales than the cell membrane.

4.4 Numerical procedures

In the numerical simulations, vertex velocities, $\boldsymbol{u}_i$, are calculated by solving the simultaneous equations of Eq. (3) for all vertices. The time evolution of the vertex locations, $\boldsymbol{r}_i$, is calculated by numerically integrating Eq. (3) using the classical Runge–Kutta method with a time step, represented by Δt. Step Δt is variable and set within a range of $2.0 \times 10^{-3}\tau$ or less, depending on the maximum velocity of vertices. The depth and width of the interface were set to the average length of the sides of the triangular elements for interfacial interaction ($d_0^{\perp} = l/2,\ d_0^{\parallel} = l/2$). Interfacial areas and interactions were computed by describing the cell surfaces and system box in octrees in order to only compare neighboring vertices.

During large deformation of the membrane, the vertex distributions can be scattered by vertex movements. To optimize the distribution, the mesh structure was dynamically rearranged using the modified remeshing algorithm [29]. The algorithm comprises three steps: 1) elimination and insertion of edges, 2) regularization of edge connectivity, and 3) centering of vertex locations. The details of the algorithm are similar to those used in our previous work [29]. The centering operation is applied to the system before every time of evolution of vertex locations. The other operators are applied before the time evolution of vertex locations at every time step, Δt_{R} $(= 10^{-2}\tau)$.

The operation of elimination and insertion of edges was performed to keep the average vertex density per area around ρ_*. The centering operation of vertex locations was slightly modified from our previously reported algorithm [29]. In this operation, the spatial distribution of the vertices was optimized by centering their locations around each vertex. To conserve the surface profile, the vertex moves only on the tangential plane through the vertex, where the drift vector of the i-th vertex is represented by $\boldsymbol{\varDelta}_i$. The length of the drift vector is limited so that its norm is less than a certain value, $|\boldsymbol{\varDelta}_i| \leq \varDelta_{\max}$. The operator is iteratively applied to each vertex to optimize the mesh structure until the drift vectors satisfy $\max_i(|\boldsymbol{\varDelta}_i|) < \varDelta_{\mathrm{th}}$, where constant $\varDelta_{\mathrm{th}}$ represents the drift threshold. The maximum drift and the drift threshold were set to be enough small as $\varDelta_{\max} = 10^{-2}l$ and $\varDelta_{\mathrm{th}} = 10^{-3}l$, respectively. Energy gaps caused by the topological operations are small enough to be ignored [29].

The numerical algorithm was implemented in C++ programming language, where OpenMP was used for parallel computations. All numerical experiments were performed on workstations with 3.2 GHz Intel Xeon dual processors and 64 GB RAM. Under the above condition, each simulation was performed over a time range of 300τ, which involved 1.5×10^5 or more steps, and the average running time was about 50 minutes.

5. Numerical simulation of long-term adherent cell dynamics under shear flow

Using the integrated model in Section 4, in this section, numerical simulations of the adherent cell dynamics on a substrate under shear flow were performed. In this situation, cell adhesion caused a large variety of cell movements, including new patterns of dynamics, i.e., cell slipping and membrane flow patterns, found in this study (Section 5.1). The observed cell movements can be quantitatively classified into five distinct patterns according to cell and membrane movements (Section 5.2). The cell shape and movement highly varied by the adhesion energy and solvent velocity (Section 5.3-5.4). By defining each pattern, we obtained the diagram of cell dynamics patterns, indicating that the long-term cell dynamics exhibited the large variety depending on the adhesion energy and solvent velocity (Section 5.5). These results showed that the proposed model enabled us to simulate the long-term dynamics of an adherent cell (Section 5.6). For the newly-found patterns of dynamics mentioned above, the features characteristic to the long-term dynamics, such as the nonelastic but frictional nature of cell-substrate adhesion and nonconservative fluid cell membrane accompanied by expansion/contraction flows [29], are essential. We analyzed the simplified model in Appendix and confirmed that such nonelastic frictional adhesion and the membrane expansion/contraction flow can indeed explain some features observed in our numerical simulations.

5.1 Variety of long-term adherent cell dynamics with membrane turnover

Figure 4 shows the typical results of the numerical simulations for various parameter values, including solvent velocity and adhesion energy. Cell dynamics varied with the solvent velocity and adhesion energy, which can be classified into several patterns based on cell and membrane motions (Fig. 4). Detachment, rolling, and fixation patterns have been reported in the previous study [25], but membrane motions in these patterns differ from those in the previous study due to the non-conservative feature of the membrane as follows. In the detachment pattern (Fig. 4a), the cell detached from the substrate and was swept forward in the solvent without adhesion. In this pattern, while the cell maintains a spherical shape, the cell membrane expanded at the rear, flowed from the rear to the front, and contracted at the front. To evaluate the membrane expansion and contraction, the area strain velocity of the membrane at the i-th triangle, represented by $\dot{\gamma}_i^{\mathrm{a}}$, was calculated by

$$\dot{\gamma}_i^{\mathrm{a}} = \frac{1}{A_i} \sum_{j(i)}^{\mathrm{vertex}} \frac{\partial A_i}{\partial \boldsymbol{r}_j} \cdot \boldsymbol{u}_j \ , \tag{29}$$

where the summation is for all vertices composing the i-th triangle. In the cell rolling pattern (Fig. 4c), the cell moved forward while rolling on the substrate. In this pattern, the cell was distorted and attached to the substrate at the rear-bottom region, where the cell membrane flowed at the cell-solvent boundary but not at the cell-substrate boundary. Along with this biased flow, the cell membrane expanded in the rear-top and front-bottom regions and contracted in the rear-bottom and front-top regions. This spatial pattern of cell membrane expansion/contraction is a natural consequence of the shear flow and the solvent friction, as studied in the Appendix with an analytical calculation of a simplified model. In the fixation pattern (Fig. 4e), the cell and membrane did not move while maintaining a semi-spherical shape.

Importantly, our simulations discovered two new patterns of adhesive dynamics, which we named cell slipping and membrane flow patterns, respectively. In the cell slipping pattern (Fig. 4b), the cell moved forward without rolling while maintaining the attachment with the substrate. During the cell movement, the cell maintained a spherical shape, and the area of attachment to the substrate was small. The cell membrane hardly flowed on the whole cell surface, including the location near the substrate. Indeed, the existence of such slipping between the cell and substrate surfaces is guaranteed also by the simplified model analysis, as long as the cell surface has non-zero viscosity and only finite strength of friction with the substrate (Appendix). In the membrane flow pattern (Fig. 4d), the cell did not move, whereas the cell membrane expanded at the rear, flowed from the rear to the front on the cell-solvent boundary, and contracted at the front.

Area strain varies depending on capillary number and adhesion energy. In the detachment state, where adhesion energy is low and capillary number is high, the rapid solvent flow causes the unidirectional flow of cell membrane, leading to area strain. When the capillary number is lower, the cell slipping state appears, where the membrane flow becomes lower with lower area strain. When adhesion energy is higher, the rolling state appears, where the membrane flow is locally suppressed by the friction on the substrate, leading to increasing area strain. Therefore, the area strain is relatively low in the cell slipping state compared to the detachment and rolling states. When either the capillary number is further lowered or the adhesion energy becomes even higher, the membrane flow state appears, where the membrane flow is locally fixed, leading to increasing area strain. When this tendency is further enhanced, the fixation state appears, where the membrane is entirely fixed, leading to the suppression of area strain.

It is to be noted that these new patterns of dynamics are found as a consequence of the proper treatments of long-term behavior. In fact, these patterns of dynamics require either a nonelastic frictional cell-substrate adhesion or a nonconservative fluid cell membrane accompanied by expansion/contraction flow (for cell slipping or membrane pattern, respectively), which are features characteristic specifically to the long-term behavior.

5.2 Quantitative characterizations of cell- and membrane-dynamics patterns

To quantitatively assess the observed patterns of adherent cell dynamics, we calculated the contact area, and cell and membrane velocities as functions of time in each pattern (Fig. 5). In order to quantify the cell adhesion to the substrate, the contact area, represented by A_{c}, was calculated, which was defined as the area of the cell-substrate boundary (Fig. 5a). While the contact area became zero in the detachment pattern, it converged into a positive value in the other patterns. To quantify the cell motion, cell velocity, represented by V_{c}, defined as the velocity of the geometric center of the cell, was calculated (Fig. 5b). While the cell velocity became zero in the membrane flow and fixation patterns, it converged into positive values in the other patterns.

To quantify the membrane flow, membrane velocity, defined as the velocity of the cell membrane along the x-axis, was calculated. The average membrane velocity, represented by $V_{\mathrm{m}}^{\mathrm{ave}}$, became zero in the fixation pattern, whereas it converged into positive values in the other patterns (Fig. 5c). To analyze whether the cell slipped or firmly adhered to the substrate, the minimum membrane velocity, represented by $V_{\mathrm{m}}^{\mathrm{min}}$, was also calculated. The minimum membrane velocity corresponded to the velocity of the membrane around the closest location to the substrate, reflecting whether the cell slipped or firmly adhered to the substrate. The minimum membrane velocity became zero in the fixation and membrane flow patterns, whereas it converged into positive values in the other patterns (Fig. 5d). These results indicated that the obtained patterns of cell dynamics can be quantitatively distinguished based on the cell and membrane movements.

5.3 Dependence of cell shape and contact on adhesion energy and solvent velocity

To investigate the influence of the cell adhesion and solvent flow on cell shape, we calculated the contact area and cell sphericity as functions of the adhesion energy, ϵ_{int}, and the capillary number, C_a (Fig. 6). The contact area depends strongly on ϵ_{int} and slightly on C_a; i.e., the area drastically increased with ϵ_{int} and slightly decreased with increasing C_a (Fig. 6a). The area became zero under the condition of small ϵ_{int} and high C_a, corresponding to the detachment pattern, and nonlinearly increased with either increasing ϵ_{int} or decreasing C_a (Fig. 6b). The cell sphericity also depends strongly on ϵ_{int} and slightly on C_a; i.e., the sphericity drastically decreased with increasing ϵ_{int}, and also decreased under the condition with high C_a (Fig. 6c). Under the condition with middle ϵ_{int} and high C_a, corresponding to the rolling pattern, the cell shape became tear-like, as reported in the previous study [25] (Fig. 6d). These results indicate that the cell shape can become semispherical, depending on the adhesion to the substrate, and it can be distorted by the solvent velocity.

5.4 Dependence of cell and membrane movements on adhesion energy and solvent velocity

To investigate the influence of the cell adhesion and solvent flow on cell and membrane movement, we calculated the cell and membrane velocities as functions of adhesion energy, ϵ_{int}, and capillary number, C_a (Fig. 7). The cell velocity became zero under the condition with high ϵ_{int} and low C_a, corresponding to the fixation pattern (Fig. 7a). The velocity increased with decreasing ϵ_{int} and increasing C_a, and became drastically high under the condition with small ϵ_{int} and high C_a, corresponding to the detachment pattern. The velocity increased from zero with decreasing ϵ_{int}, whose slopes became steeper with increasing C_a (Fig. 7b).

Moreover, the average and minimum membrane velocities became zero under the condition with high ϵ_{int} and low C_a (Fig. 7c-d). They increased with decreasing ϵ_{int} and increasing C_a, and became extremely high under the condition with small ϵ_{int} and high C_a, corresponding to the detachment pattern. Notably, minimum membrane velocity is relatively high under the condition with small ϵ_{int} and middle C_a, corresponding to the cell slipping pattern. The average and minimum membrane velocities converged to zero with increasing ϵ_{int} and their slopes became steeper with increasing C_a (Fig. 7e-f). Importantly, the cell and average membrane velocities were accelerated by both the decrease in ϵ_{int} and increase in C_a, whereas the minimum membrane velocity was increased only under the condition with low adhesion, corresponding to the cell slipping pattern.

5.5 Pattern diagram of cell dynamics with respect to adhesion energy and solvent velocity

To assess the dependence of cell dynamics patterns on cell adhesion and solvent flow, we quantitatively defined each pattern, based on the results given in Section 5.2, in terms of the contact area, A_{c}, cell velocity, V_{c}, and minimum membrane velocity, $V_{\mathrm{m}}^{\mathrm{min}}$ (Table 2). The detachment pattern is defined as the condition when the contact area is zero ($A_{\mathrm{c}} = 0$). The cell slipping pattern is defined as the condition that both the cell velocity and minimum membrane velocity are positive ($A_{\mathrm{c}} > 0,\ V_{\mathrm{c}} \geq \delta V,\ V_{\mathrm{m}}^{\mathrm{min}} \geq \delta V$). The rolling pattern is when the cell velocity is positive and the minimum membrane velocity is almost zero ($A_{\mathrm{c}} > 0,\ V_{\mathrm{c}} \geq \delta V,\ V_{\mathrm{m}}^{\mathrm{min}} < \delta V$). Moreover, the membrane flow is when the cell velocity is almost zero and membrane velocity is positive ($A_{\mathrm{c}} > 0,\ V_{\mathrm{c}} < \delta V,\ V_{\mathrm{m}}^{\mathrm{min}} \geq \delta V$), and the fixation pattern is when both cell velocity and membrane velocity are almost zero ($A_{\mathrm{c}} > 0,\ V_{\mathrm{c}} < \delta V,\ V_{\mathrm{m}}^{\mathrm{min}} < \delta V$). Here, δV indicates a small threshold velocity, which was set to $\delta V = 0.2\ \ l/\tau$.

Based on these definitions of each pattern, the pattern diagram of cell dynamics was obtained (Fig. 8). While the fixation pattern was obtained under the condition with high ϵ_{int} and low C_a, the detachment pattern was obtained under the condition with low ϵ_{int} and high C_a. The other patterns were obtained between these two conditions as follows: The cell slipping pattern was obtained under the condition with low ϵ_{int} and intermediate C_a. When increasing ϵ_{int} from the cell slipping pattern, the cell dynamics transited to the rolling. For further increase in ϵ_{int}, membrane flow and fixation patterns appear in that order. While either the membrane flow or rolling pattern was beside the fixation pattern, either the cell slipping or rolling pattern was sided by the detachment pattern. Thus, these results show that long-term cell dynamics are highly variable, depending on cell adhesion and solvent flow.

Various quantitative features of the resultant cell shape and dynamics showed only smooth dependencies on ϵ_{int} and C_a (Figs. 6-7), suggesting that all these crossovers between individual patterns, except for the detachment pattern, are not a bifurcation but a gradual crossover. In particular, the gradual crossover between cell slipping and rolling was also supported by the simple-model analysis (Appendix).

5.6 Mechanisms of long-term adherent cell dynamics under flow

Cell states were determined by the balance between adhesion force on the substrate and friction force from the solvent shear flow, i.e., adhesion generates friction and adsorption on the cell bottom, whereas solvent shear flow generates drag and lift force. In particular, in the simplified flow field of this study (Sect. 4.2), the lift force is generated by the asymmetry of the cell shape along the solvent flow direction. For example, when the cell is spherical, the friction force is balanced across the entire cell surface, generating no lift force. On the other hand, as an extreme example, when the cell has a linear shape aligned in a frontal lifted direction, the friction force is imbalanced to generate a lift force. Remember that our model takes into account membrane viscosity; hence the competition between membrane viscosity and solvent friction generates not only upward flow of the membrane, but also a lift force across the membrane. Because the cell is aligned in a frontal lifted direction by the solvent shear flow, the cell is thus subject to lift force.

Mechanisms that cause the fixation, rolling, and detachment patterns can be explained basically as in the previous study [25]; i.e., the increase in C_a corresponds to the increase in lift force with increasing solvent velocity, leading to the detachment pattern [44]. Less C_a with middle ϵ_{int} generates low lift force but enough high drag force, leading to the rolling pattern [25,45,46]. Either lower C_a or higher ϵ_{int} suppresses drag force, leading to the fixation pattern [25]. In the previous study, where relatively short-term cell dynamics were calculated by assuming an elastic membrane, cell dynamics patterns transited from the fixation to either the detachment or rolling [25]. In contrast, in this study, where long-term cell dynamics were calculated by assuming a nonconservative fluid membrane and nonelastic frictional adhesion, the cell slipping and membrane flow appeared at the interface among the fixation, detachment, and rolling (Fig. 8).

Mechanisms that cause the cell slipping and membrane flow can be explained by frictional interactions at the cell-substrate interface. The cell slipping can be provided under the condition with low ϵ_{int}, since the cell-substrate friction can be much lower than the cell membrane viscosity. Under this condition, both the cell-substrate and cell-solvent interfaces can move faster than the membrane flow, leading to the cell slipping. Membrane flow can be provided near the fixation pattern, where both the lift and drag forces are fully suppressed by adhesion. Either when C_a is relatively high or ϵ_{int} is relatively low, the drift force can barely move the membrane. However, because the cell-substrate friction is much lower than the cell membrane viscosity, the membrane can move only partially at the cell-solvent interface, leading to the membrane flow. In principle, the cell slipping could be provided by the elastic membrane but not the membrane flow, since the membrane flow requires the nonconservative feature. These results illustrate that adherent cell dynamics are more diverse on the long-term than on the short-term scale, where frictional interfacial interactions play a key role.

6. Discussion

In this paper, we aimed to computationally investigate the possible patterns of long-term adherent cell dynamics occurring in a whole cell or in multicellular systems. We firstly developed a continuum model of energetic and frictional interfacial interaction between discrete surfaces for numerical simulations. We then integrated this interaction model with the model of nonconservative fluid cell membrane [29] and performed numerical simulations of adherent cell dynamics on substrate under flow. The simulations showed that adherent cell dynamics exhibited five distinct patterns, i.e., detachment, cell slipping, rolling, membrane flow, and fixation.

Importantly, while the detachment, rolling, and fixation patterns were also observed in the previous study [25], the membrane flow and cell slipping patterns were newly found in this study. This stark difference in the results provides us with the following important lessons. The membrane flow and cell slipping patterns correspond to the cell behaviors occurring in the long-term, where the cell membrane can dynamically turnover via endocytosis and exocytosis and CAMs frequently bind and unbind, i.e., the cell membrane is nonconservative and the cell and substrate do not firmly adhere but can move with the friction derived from the CAMs remodeling. On the other hand, in most previous studies, relatively short-term cell behaviors were focused on, where the cell membrane is an elastic body and CAMs can firmly fix a cell on substrate [25]. This is why the simulations in this paper succeeded in simulating the wider varieties of long-term adherent cell dynamics including the membrane flow and cell slipping patterns while the simulations in previous studies did not. This implies that it is pivotal to use the model reflecting the scale of time properly, i.e., the model taking into account nonconservative cell membrane and frictional adhesion, when one simulates the long-term adherent cell dynamics.

In the proposed model, interfacial interactions between surfaces are expressed by energetic and frictional interactions, and their parameters are given as those in the continuum level, i.e., adhesion energy and friction. Importantly, these parameters in the continuum level can be quantitatively translated into those at the molecular level such as CAM density, individual-CAM adhesion energy, and association and dissociation rates, which are experimentally measurable parameters. Therefore, the proposed model enables us to predict realistic adherent cell dynamics in a quantitative manner. Importantly, the friction is explicitly described in the proposed model, whereas it was implicitly taken into account in the previous studies [27]. In the previous studies, adhesion was modeled by the association and dissociation behaviors of the spring bonds linking two surfaces. The explicit description in the proposed model enables us to quantitatively analyze the long-term cell dynamics. Note that although we derived the effects of the friction via CAM behaviors as the strain rate ϕ_{int}, its detailed influence, i.e., how interfacial frictions affect the adherent cell dynamics, is not yet known and this is a challenging question for the future.

The proposed model has several avenues for application and further improvement. One of the most fascinating applications is multicellular dynamics. While the model was applied to cell-substrate adhesion in this study, in principle, it can also be applied to cell-cell adhesion. This application enables us to analyze how individual-cell behaviors are integrated into multicellular dynamics through their adhesive interactions in tissues or multicellular assemblies like organoids. To analyze multicellular dynamics in 3D space, recently, several simpler coarse-grained models have been used, such as vertex models [14,15,47,48]. In addition, a recent pioneering work reported the analysis of adhesive multicellular dynamics, where individual cell membranes are represented as elastic bodies [28]. The proposed model, applicable to the long-term dynamic process in the subcellular resolution, newly enables us to analyze long-term multicellular phenomena such as embryogenesis, carcinogenesis, immune defense, and wound healing. Moreover, because cytoskeletal dynamics play important roles in cell dynamics, combining cytoskeletal dynamics with cell adhesion is an expected direction to improve the proposed model. For example, actin cytoskeletons can be bonded with CAMs, which can be stabilized by exerted tension [49,50]. These improvements enable us to simulate cell dynamics in realistic scenarios, such as cell spreading and migration on a substrate.

7. Conclusion

Cell adhesion plays key roles in development, immune defense, wound healing, and cancer invasion, which have time scales ranging from tens of minutes to days. This paper reported, firstly, the development of a computational model applicable to simulate such long-term dynamics of adherent cells and, secondly, the numerical discovery of the patterns of adherent cell dynamics characteristic to the long-term dynamics. The model is based on a continuum description of the cell surface and incorporates the energetic and frictional interactions between adhesive surfaces. With this model, the adherent cell dynamics on a solid substrate under shear flow were numerically simulated. The simulations reproduced several patterns of adherent cell dynamics, some of which were newly discovered in this study, corresponding to the behaviors occurring in the time scale much longer than that of the dissociation of adhesion molecules. These results imply that to simulate the long-term adherent cell dynamics, a model properly dealing with the nonconservative fluid cell membrane and nonelastic frictional adhesion is necessary. The model developed in this paper can be applied to further realistic phenomena by introducing the dynamics of cytoskeletal components and extracellular matrices, and has the potential to be applicable to simulating the dynamics of tissues or multicellular assemblies like organoids.

Author Contribution

SO conceived the project, developed the software, and performed the analyses; TH provided ideas and analytical solution in Appendix; SO wrote the first draft of the manuscript, and SO and TH reviewed and edited. All authors contributed to the final manuscript.

Conflict of interest

There are no conflicts to declare.

Acknowledgment

We thank to Dr. Alexander S. Mikhailov at Kanazawa University for discussions. This work was supported by the Japan Science and Technology Agency (JST), CREST Grant No. JPMJCR1921; the Japan Agency for Medical Research and Development (AMED), Grant No. 21bm0704065h0002; the Japan Society for the Promotion of Science (JSPS), KAKENHI Grants No. 21H01209, 22K18749, and 22H05170; the World Premier International Research Center Initiative, Ministry of Education, Culture, Sports, Science and Technology (MEXT), Japan (to SO); and the seed grant of Mechanobiology Institute (to TH)

References

[1] P. Chugh and E. K. Paluch, *The Actin Cortex at a Glance*, J Cell Sci **131**, jcs186254 (2018).

[2] J. C. Dallon, E. Newren, and M. D. H. Hansen, *Using a Mathematical Model of Cadherin-Based Adhesion to Understand the Function of the Actin Cytoskeleton*, Phys Rev E **79**, 31918 (2009).

[3] I. Indra, J. Choi, C.-S. Chen, R. B. Troyanovsky, L. Shapiro, B. Honig, and S. M. Troyanovsky, *Spatial and Temporal Organization of Cadherin in Punctate Adherens Junctions*, Proceedings of the National Academy of Sciences **115**, E4406 (2018).

[4] J. Silvestre, P. J. A. Kenis, and D. E. Leckband, *Cadherin and Integrin Regulation of Epithelial Cell Migration*, Langmuir **25**, 10092 (2009).

[5] Q. Shi, Y.-H. Chien, and D. Leckband, *Biophysical Properties of Cadherin Bonds Do Not Predict Cell Sorting*, Journal of Biological Chemistry **283**, 28454 (2008).

[6] Y. Liu and W. K. Liu, *Rheology of Red Blood Cell Aggregation by Computer Simulation*, J Comput Phys **220**, 139 (2006).

[7] C. A. Brebbia, J. C. F. Telles, and L. C. Wrobel, *Boundary Element Techniques: Theory and Applications in Engineering* (Springer Science & Business Media, 2012).

[8] C. Pozrikidis and others, *Boundary Integral and Singularity Methods for Linearized Viscous Flow* (Cambridge university press, 1992).

[9] S. Kim and S. J. Karrila, *Microhydrodynamics: Principles and Selected Applications* (Courier Corporation, 2013).

[10] H. J. Kim et al., *Time-Evolving Genetic Networks Reveal a NAC Troika That Negatively Regulates Leaf Senescence in Arabidopsis*, Proceedings of the National Academy of Sciences **115**, E4930 (2018).

[11] M.-C. Kim, D. M. Neal, R. D. Kamm, and H. H. Asada, *Dynamic Modeling of Cell Migration and Spreading Behaviors on Fibronectin Coated Planar Substrates and Micropatterned Geometries*, PLoS Comput Biol **9**, e1002926 (2013).

[12] K. Tsubota, S. Wada, and T. Yamaguchi, *Particle Method for Computer Simulation of Red Blood Cell Motion in Blood Flow*, Comput Methods Programs Biomed **83**, 139 (2006).

[13] J. Mauer, S. Mendez, L. Lanotte, F. Nicoud, M. Abkarian, G. Gompper, and D. A. Fedosov, *Flow-Induced Transitions of Red Blood Cell Shapes under Shear*, Phys Rev Lett **121**, 118103 (2018).

[14] S. Okuda, Y. Inoue, M. Eiraku, T. Adachi, and Y. Sasai, *Vertex Dynamics Simulations of Viscosity-Dependent Deformation during Tissue Morphogenesis*, Biomech Model Mechanobiol **14**, 413 (2015).

[15] H. Honda, M. Tanemura, and T. Nagai, *A Three-Dimensional Vertex Dynamics Cell Model of Space-Filling Polyhedra Simulating Cell Behavior in a Cell Aggregate*, J Theor Biol **226**, 439 (2004).

[16] M. Akiyama, M. Nonomura, A. Tero, and R. Kobayashi, *Numerical Study on Spindle Positioning Using Phase Field Method*, Phys Biol **16**, (2019).

[17] M. Nonomura, *Study on Multicellular Systems Using a Phase Field Model*, PLoS One **7**, (2012).

[18] N. Saito and S. Sawai, *Three-Dimensional Morphodynamic Simulations of Macropinocytic Cups*, IScience **24**, 103087 (2021).

[19] K. Fuji, S. Tanida, M. Sano, M. Nonomura, D. Riveline, H. Honda, and T. Hiraiwa, *Computational Approaches for Simulating Luminogenesis*, in *Seminars in Cell & Developmental Biology* (2022).

[20] B. Cerruti et al., *Polarity, Cell Division, and out-of-Equilibrium Dynamics Control the Growth of Epithelial Structures*, Journal of Cell Biology **203**, 359 (2013).

[21] I. Fortuna, G. C. Perrone, M. S. Krug, E. Susin, J. M. Belmonte, G. L. Thomas, J. A. Glazier, and R. M. C. de Almeida, *CompuCell3D Simulations Reproduce Mesenchymal Cell Migration on Flat Substrates*, Biophys J **118**, 2801 (2020).

[22] T. Hirashima, E. G. Rens, and R. M. H. Merks, *Cellular Potts Modeling of Complex Multicellular Behaviors in Tissue Morphogenesis*, Dev Growth Differ **59**, 329 (2017).

[23] D. A. Hammer and S. M. Apte, *Simulation of Cell Rolling and Adhesion on Surfaces in Shear Flow: General Results and Analysis of Selectin-Mediated Neutrophil Adhesion*, Biophys J **63**, 35 (1992).

[24] D. A. Hammer, *Adhesive Dynamics*, J Biomech Eng **136**, 21006 (2014).

[25] Z. Zhang, J. Du, Z. Wei, Z. Wang, and M. Li, *Effects of Membrane Deformability and Bond Formation/Dissociation Rates on Adhesion Dynamics of a Spherical Capsule in Shear Flow*, Biomech Model Mechanobiol **17**, 223 (2018).

[26] S. Wang, T. Ye, G. Li, X. Zhang, and H. Shi, *Margination and Adhesion Dynamics of Tumor Cells in a Real Microvascular Network*, PLoS Comput Biol **17**, e1008746 (2021).

[27] T. Odenthal, B. Smeets, P. van Liedekerke, E. Tijskens, H. van Oosterwyck, and H. Ramon, *Analysis of Initial Cell Spreading Using Mechanistic Contact Formulations for a Deformable Cell Model*, PLoS Comput Biol **9**, e1003267 (2013).

[28] P. van Liedekerke, J. Neitsch, T. Johann, E. Warmt, I. Gonzàlez-Valverde, S. Hoehme, S. Grosser, J. Kaes, and D. Drasdo, *A Quantitative High-Resolution Computational Mechanics Cell Model for Growing and Regenerating Tissues*, Biomech Model Mechanobiol **19**, 189 (2020).

[29] S. Okuda, K. Sato, and T. Hiraiwa, *Continuum Modeling of Non-Conservative Fluid Membrane for Simulating Long-Term Cell Dynamics*, The European Physical Journal E **45**, 69 (2022).

[30] M. Belkin, J. Sun, and Y. Wang, *Discrete Laplace Operator on Meshed Surfaces*, in *Proceedings of the Twenty-Fourth Annual Symposium on Computational Geometry* (2008), pp. 278–287.

[31] See Supplemental Material at [URL will be inserted by publisher] for [give brief description of material].

[32] R. D. Groot and P. B. Warren, *Dissipative Particle Dynamics: Bridging the Gap between Atomistic and Mesoscopic Simulation*, J Chem Phys **107**, 4423 (1997).

[33] K. Tawada and K. Sekimoto, *Protein Friction Exerted by Motor Enzymes through a Weak-Binding Interaction*, J Theor Biol **150**, 193 (1991).

[34] B. Majhy, P. Priyadarshini, and A. K. Sen, *Effect of Surface Energy and Roughness on Cell Adhesion and Growth–Facile Surface Modification for Enhanced Cell Culture*, RSC Adv **11**, 15467 (2021).

[35] G. Salbreux, G. Charras, and E. Paluch, *Actin Cortex Mechanics and Cellular Morphogenesis*, Trends Cell Biol **22**, 536 (2012).

[36] E. Fischer-Friedrich, A. A. Hyman, F. Jülicher, D. J. Müller, and J. Helenius, *Quantification of Surface Tension and Internal Pressure Generated by Single Mitotic Cells*, Sci Rep **4**, 1 (2014).

[37] M. Fritzsche, A. Lewalle, T. Duke, K. Kruse, and G. Charras, *Analysis of Turnover Dynamics of the Submembranous Actin Cortex*, Mol Biol Cell **24**, 757 (2013).

[38] S. Mukhina, Y. Wang, and M. Murata-Hori, *α-Actinin Is Required for Tightly Regulated Remodeling of the Actin Cortical Network during Cytokinesis*, Dev Cell **13**, 554 (2007).

[39] A. K. Prakasam, V. Maruthamuthu, and D. E. Leckband, *Similarities between Heterophilic and Homophilic Cadherin Adhesion*, Proceedings of the National Academy of Sciences **103**, 15434 (2006).

[40] B. L. Neel, C. R. Nisler, S. Walujkar, R. Araya-Secchi, and M. Sotomayor, *Collective Mechanical Responses of Cadherin-Based Adhesive Junctions as Predicted by Simulations*, Biophys J **121**, 991 (2022).

[41] E. Perret, A.-M. Benoliel, P. Nassoy, A. Pierres, V. Delmas, J.-P. Thiery, P. Bongrand, and H. Feracci, *Fast Dissociation Kinetics between Individual E-Cadherin Fragments Revealed by Flow Chamber Analysis*, EMBO J **21**, 2537 (2002).

[42] S. Rakshit, Y. Zhang, K. Manibog, O. Shafraz, and S. Sivasankar, *Ideal, Catch, and Slip Bonds in Cadherin Adhesion*, Proceedings of the National Academy of Sciences **109**, 18815 (2012).

[43] D. Häussinger, T. Ahrens, T. Aberle, J. Engel, J. Stetefeld, and S. Grzesiek, *Proteolytic E-Cadherin Activation Followed by Solution NMR and X-Ray Crystallography*, EMBO J **23**, 1699 (2004).

[44] M. Abkarian, C. Lartigue, and A. Viallat, *Tank Treading and Unbinding of Deformable Vesicles in Shear Flow: Determination of the Lift Force*, Phys Rev Lett **88**, 68103 (2002).

[45] S. Jadhav, C. D. Eggleton, and K. Konstantopoulos, *A 3-D Computational Model Predicts That Cell Deformation Affects Selectin-Mediated Leukocyte Rolling*, Biophys J **88**, 96 (2005).

[46] V. Pappu and P. Bagchi, *3D Computational Modeling and Simulation of Leukocyte Rolling Adhesion and Deformation*, Comput Biol Med **38**, 738 (2008).

[47] S. Okuda, E. Kuranaga, and K. Sato, *Apical Junctional Fluctuations Lead to Cell Flow While Maintaining Epithelial Integrity*, Biophys J **116**, 1159 (2019).

[48] S. Okuda, K. Unoki, M. Eiraku, and K. Tsubota, *Contractile Actin Belt and Mesh Structures Provide the Opposite Dependence of Epithelial Stiffness on the Spontaneous Curvature of Constituent Cells*, Dev Growth Differ **59**, 455 (2017).

[49] M. Cavey, M. Rauzi, P.-F. Lenne, and T. Lecuit, *A Two-Tiered Mechanism for Stabilization and Immobilization of E-Cadherin*, Nature **453**, 751 (2008).

[50] J. Slováková, M. Sikora, F. N. Arslan, S. Caballero-Mancebo, S. F. G. Krens, W. A. Kaufmann, J. Merrin, and C.-P. Heisenberg, *Tension-Dependent Stabilization of E-Cadherin Limits Cell–Cell Contact Expansion in Zebrafish Germ-Layer Progenitor Cells*, Proceedings of the National Academy of Sciences **119**, e2122030119 (2022).

Tables

Table 1: Physical parameters for numerical simulations

Parameter	Unit	Explanation
l	-	Edge length (set to be a unit)
Γ	-	Cortical tension of cell membrane (set to be a unit)
μ	-	Planar viscosity of cell membrane (set to be a unit)
L_x, L_y, L_z	l	System box size ($= 50, 52, 30$)
V_{ref}	l^3	Reference cell volume ($= 10^3$)
ξ_{e}	μ	Friction density coefficient from solvent ($= 10^{-3}$)
K	Γl^2	Cell volume elasticity ($= 10^5$)
φ_{int}	l^2/τ	Constant for interface property ($= 10^{-2}$)
C_a	$-$	Capillary number
ϵ_{int}	Γ	Interfacial energy
$\boldsymbol{u}$	l/τ	Membrane velocity
$\dot{\gamma}_i^{\mathrm{a}}$	l^2/τ	Area strain velocity
A_{c}	l^2	Contact area
V_{c}	l/τ	Cell velocity
$V_{\mathrm{m}}^{\mathrm{ave}}$	l/τ	Average membrane velocity
$V_{\mathrm{m}}^{\mathrm{min}}$	l/τ	Minimum membrane velocity
Δt	τ	Time step of vertex displacements ($= 2.0 \times 10^{-3}$)
Δt_{R}	τ	Time step of topological operations ($= 10^{-2}$)
$d_0^{\perp}$	l	Depth of interface ($= 1/2$)
$d_0^{\parallel}$	l	Width of interface ($= 1/2$)

$\mathit{\Delta}_{\mathrm{max}}$	l	Maximum value of drift ($= 10^{-2}$)
$\mathit{\Delta}_{\mathrm{th}}$	l	Drift threshold ($= 10^{-3}$)
$V_{\mathrm{m}}^{\mathrm{min}}$	l/τ	Minimum membrane velocity

Table 2: Classification of adherent cell dynamics patterns

Pattern	Contact area	Cell velocity	Membrane velocity
Detachment	$A_{\mathrm{c}} = 0$	-	-
Cell slipping	$A_{\mathrm{c}} > 0$	$V_{\mathrm{c}} \geq \delta V$	$V_{\mathrm{m}}^{\mathrm{min}} \geq \delta V$
Rolling			$V_{\mathrm{m}}^{\mathrm{min}} < \delta V$
Membrane flow		$V_{\mathrm{c}} < \delta V$	$V_{\mathrm{m}}^{\mathrm{min}} \geq \delta V$
Fixation			$V_{\mathrm{m}}^{\mathrm{min}} < \delta V$

Figures

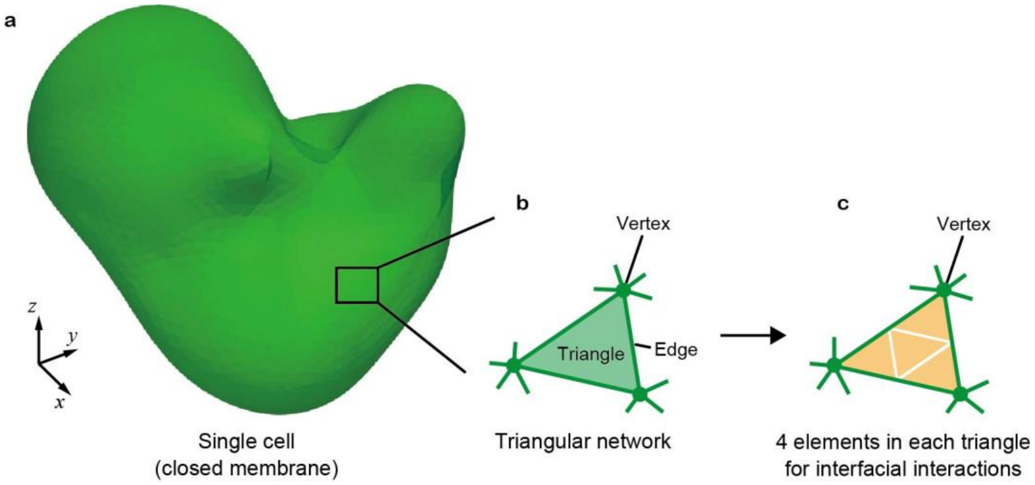

Fig. 1: Discrete description of cell surface membrane in three dimensions.

a. Single cell shape with a closed membrane. **b.** Triangular mesh describing a cell shape. Vertices and edges are shared with neighboring triangles. **c.** Four triangular elements in each triangular mesh for describing interfacial interactions. The triangle is divided by line segments connecting the bisector points of the edges.

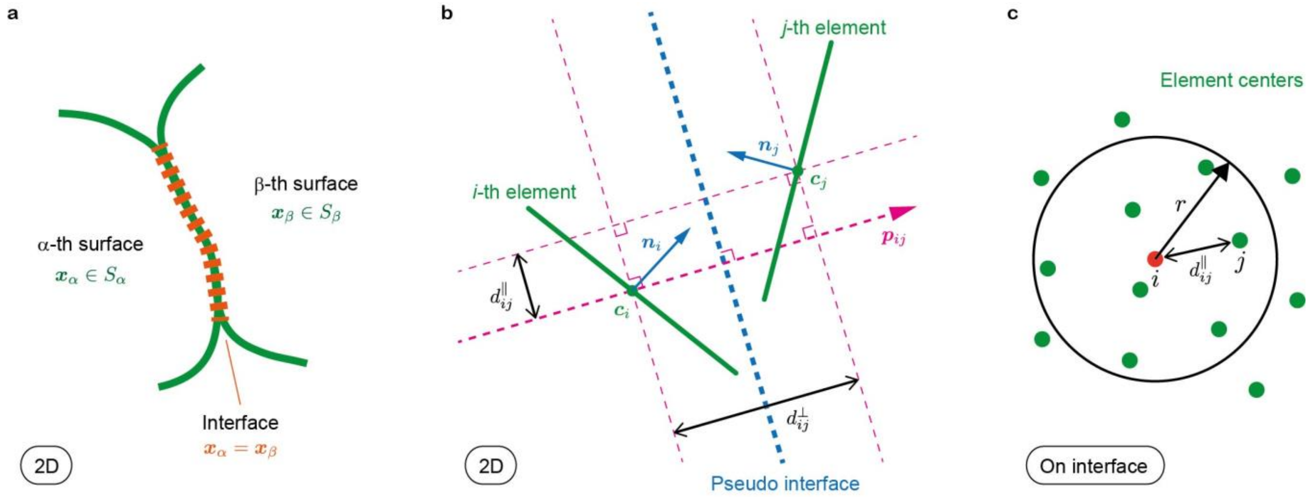

Fig. 2: Description of interface between adhesive surfaces.

a. Interface between surfaces in a 2D description. The α-th and β-th surfaces are represented by S_α and S_β, on which position vectors are represented by $\boldsymbol{x}_\alpha$ and $\boldsymbol{x}_\beta$, respectively. These surfaces form an interface at the position where cell surfaces overlap ($\boldsymbol{x}_\alpha = \boldsymbol{x}_\beta$). **b.** Interface between elements in a 2D description. The i-th and j-th elements form a pseudo interface, represented by H_{ij}, whose normal vector is represented by $\boldsymbol{p}_{ij}$. Center vectors and normal vectors of the i-th and j-th elements are represented by $\boldsymbol{c}_i$, $\boldsymbol{c}_j$, $\boldsymbol{n}_i$ and $\boldsymbol{n}_j$, respectively. The distance between the i-th and j-th elements is separated into its normal and tangential components, represented by $d_{ij}^{\perp}$ and $d_{ij}^{\parallel}$, respectively. **c.** Interaction between elements at the interface between two planar surfaces. Here, the contribution to the i-th element of one surface (red) from the j-th elements of the other surface (green) is considered. The distance from the i-th is represented by r.

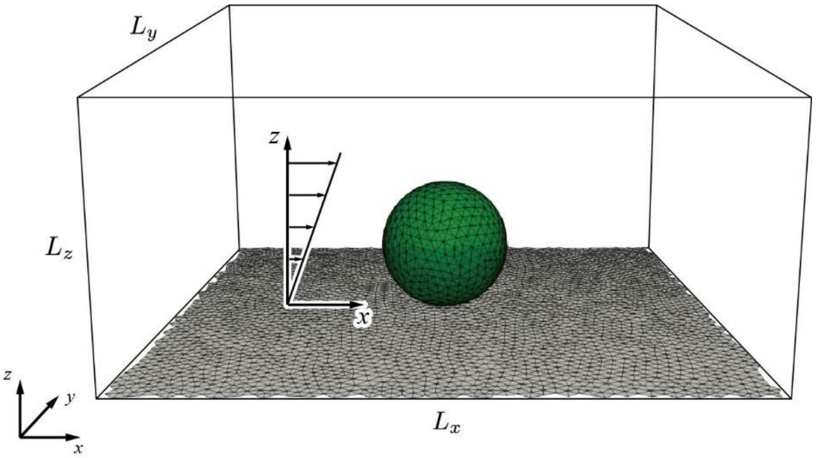

Fig. 3 Adherent cell on substrate under shear flow

The system box was considered, which is rectangular within $0 \leq x \leq L_x$, $0 \leq y \leq L_y$, and $0 \leq z \leq L_z$ in the orthogonal xyz-coordinates. Periodic boundary conditions were applied to the boundary planes. A solid substrate was located at $z = 0$ in the xy-plane, whose vertex locations were fixed in the coordinates. Under the initial condition, a single cell with a spherical shape was located on the substrate.

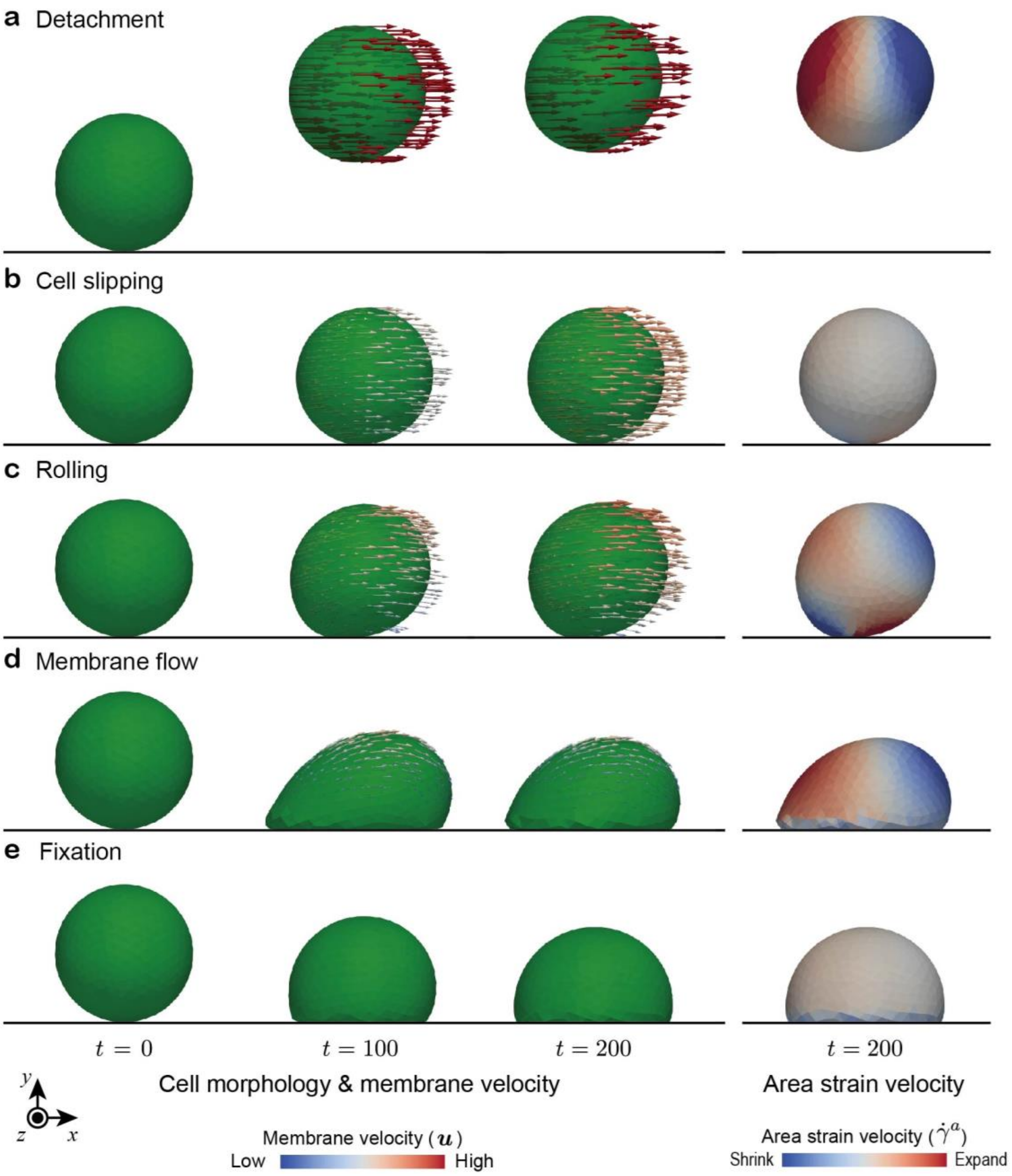

Fig. 4 Distinctive pattern of adherent cell dynamics on substrate under flow.

Five distinctive patterns of cell dynamics were observed, i.e., detachment, cell slipping, rolling, membrane flow, and fixation. **a)** Detachment, where the cell detached from substrate. **b)** Cell slipping, where the cell moved as sliding on substrate. **c)** Rolling, where the cell moved on substrate while rolling on substrate. **d)** Membrane flow, where the cell was fixed on substrate while the membrane flowed. **e)** Fixation, where the cell was fixed on substrate without membrane flow. The left panels side indicate the time evolution of cell shape, where arrows indicate local membrane velocities and their colors mean the velocity magnitudes, as indicated by the color code shown at the bottom. The right panels indicate area strain velocities at the steady state (t = 200) using the color code shown at the bottom. The parameters were set to $C_a = 10^{-1.2}$ and $\epsilon_{\text{int}} = 10^{-3}\ \Gamma l^2$ in **a**, $C_a = 10^{-1.2}$ and $\epsilon_{\text{int}} = 10^{1}\ \Gamma l^2$ in **b**, $C_a = 10^{-1.7}$ and $\epsilon_{\text{int}} = 10^{-2}\ \Gamma l^2$ in **c**, $C_a = 10^{-2.2}$ and $\epsilon_{\text{int}} = 10^{-3}\ \Gamma l^2$ in **d**, and $C_a = 10^{-2.2}$ and $\epsilon_{\text{int}} = 10^{1}\ \Gamma l^2$ in **e**.

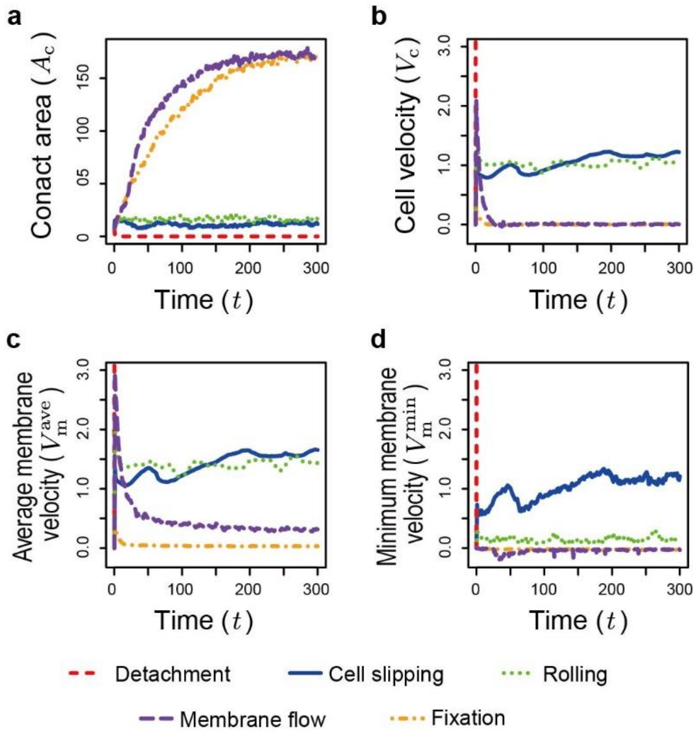

Fig. 5 Time evolution of adherent cell movement under flow.

a) Contact area of the cell on substrate, A_c, **b)** cell velocity along the x-axis, V_c, , **c)** membrane velocity along the x-axis, V_m^{ave}, and **d)** minimum membrane velocity along the x-axis, V_m^{min}, as functions of time. The parameters used for these simulations were set to those used in Fig. 4.

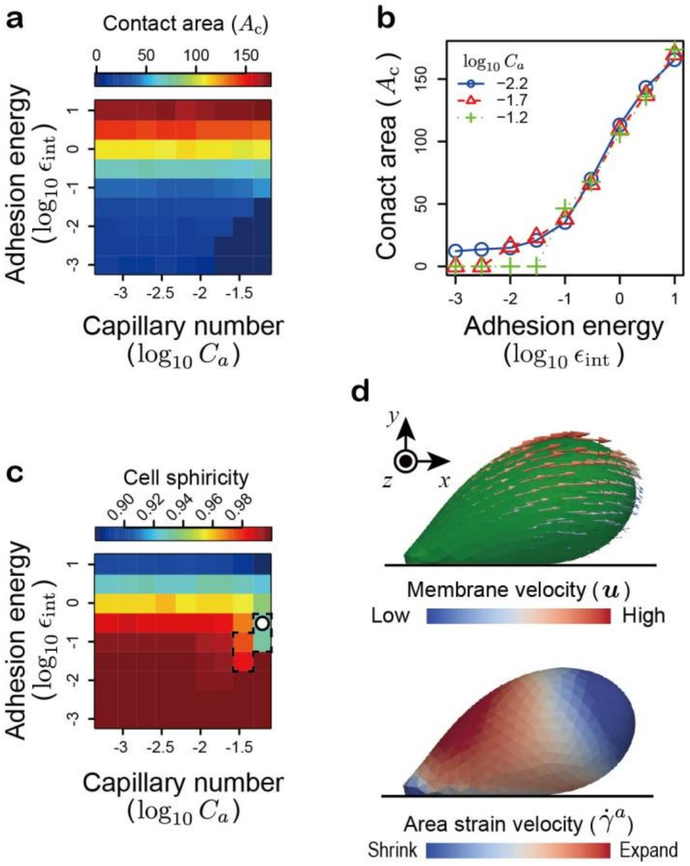

Fig. 6 Dependence of cell shape and contact on capillary number and adhesion energy

a-b) Contact area, $A_{\rm c}$, as a function of adhesion energy and capillary number. Blue, red, and green lines in **b** indicate the conditions with $C_a = 10^{-2.2}$, $10^{-1.7}$, and $10^{-1.2}$, respectively. **c)** Sphericity of the cell on the substrate as a function of adhesion energy and capillary number. **d)** Tear-like shape of the cell. The panel on the left-hand side indicates the cell shape, where arrows indicate local membrane velocities. The panel on the right-hand side indicates area strain velocities. The parameters were set to $C_a = 10^{-1.2}$ and $\epsilon_{\rm int} = 10^{-0.5}\ \Gamma l^2$ in **d**.

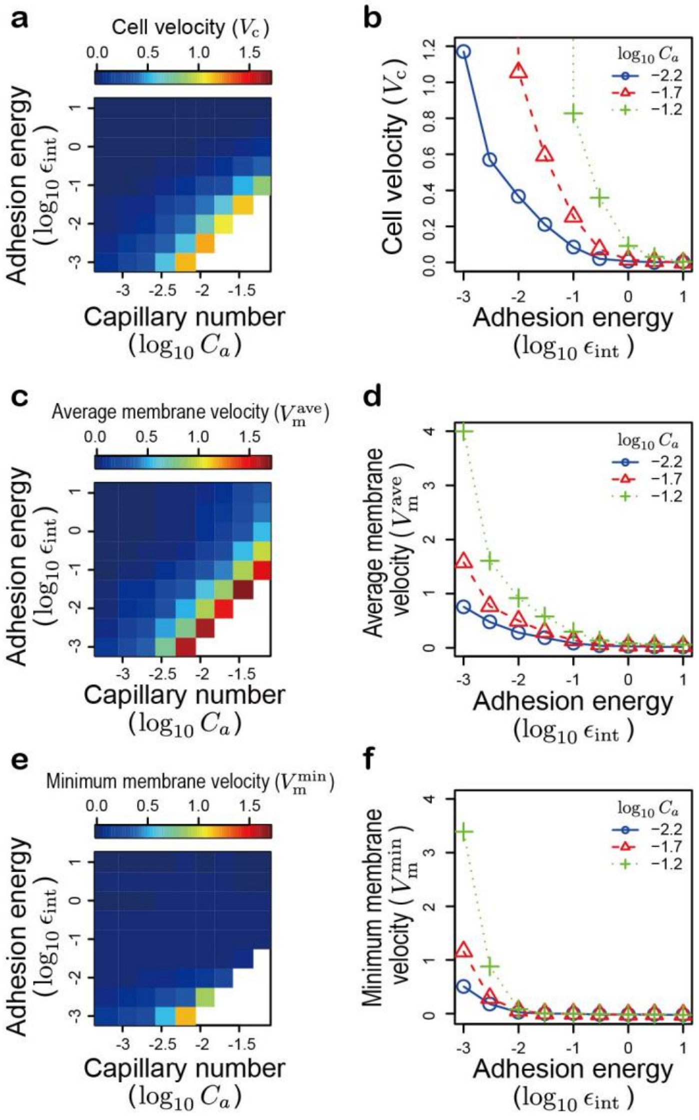

Fig. 7 Dependence of cell and membrane movements on capillary number and adhesion energy

a-b) Cell velocity along the *x*-axis, V_{c}, as a function of adhesion energy and capillary number. **c-d)** Average membrane velocity along the *x*-axis, $V_{\mathrm{m}}^{\mathrm{ave}}$, as a function of adhesion energy and capillary number. **e-f)** Minimum membrane velocity along the *x*-axis, $V_{\mathrm{m}}^{\mathrm{min}}$, as a function of adhesion energy and capillary number. Blue, red, and green lines in **b**, **d**, and **f** indicate the conditions with $C_a = 10^{-2.2}$, $10^{-1.7}$, and $10^{-1.2}$, respectively. The white regions in **a**, **c**, and **e** indicate those with values above the maximums of the legend colormaps.

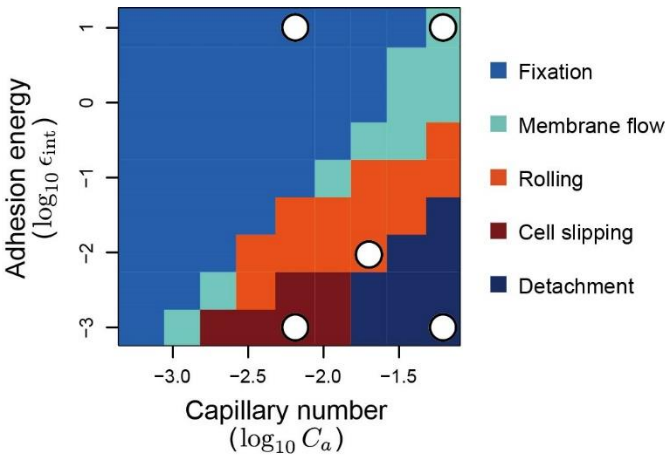

Fig. 8 Diagram of adherent cell dynamics patterns

The pattern diagram of adherent cell dynamics was calculated as a function of capillary number C_a and adhesion energy ϵ_{int}. White circles correspond to the results in Figs. 4 and 5.